Comparison of Cascade, Lattice, and Parallel Filter Architectures

Rohit Patnaik, Vivek Vandrasi, Christi K. Madsen, Ali A. Eftekhar, and Ali Adibi

***Abstract*—We examine the use of different high-level filter architectures (cascade, lattice, and parallel). We discuss their advantages and disadvantages, and we present simulation results and filter-tolerance tests. This information serves as a useful comparative analysis in the selection of a high-level filter architecture for a particular problem. The sensitivity to nonlinearity is also evaluated as resonance-enhanced power in the feedback path. For narrowband band-pass responses, cascade architectures appear to be more tolerant to filter parameter variations than lattice architectures and are substantially more efficient than parallel architectures.**

***Index Terms*—Cascade filter, filter architecture, filter tolerance, lattice filter, parallel filter.**

I. Introduction

ONE can design optical filters using different filter architectures. Examples include the all-pass sum–difference architecture [1] and the lattice architecture [2]. In this paper, we analyze these and other high-level architectures (that are similar to the ones in [3]). We discuss their advantages and disadvantages in terms of ease of parameter selection. We present tolerance test results for variations in the filter parameters. Since nonlinearity is an important concern in the operation of optical filters, we also compare the expected degree of nonlinearity for the different high-level architectures. The analysis presented in this paper should serve as a useful tool when one is selecting a high-level filter architecture for a particular problem.

II. Theory

A. High-Level Digital Building Block

Our high-level digital building block is shown in Fig. 1. This digital building block is used in all of our high-level digital filter architectures. In Fig. 1 , there is a symmetric Mach–Zehnder interferometer (MZI) with an all-pass filter in each arm. The order of the digital building block M is the total number of poles (or zeros). Both $A_U(z)$ and $A_L(z)$ have unity gain and are of order $M/2$. Since $A_U(z)$ and $A_L(z)$ are all-pass filters, they are completely specified by their pole magnitudes and phases. The poles of $A_L(z)$ are selected to be the complex conjugates of the poles of $A_U(z)$. This ensures that the magnitude response for the digital building block is symmetric about the central frequency. There are also constant phase terms β and $-\beta$ in the upper and lower arms, respectively, of the MZI. These set the zeros of the digital building block. A constant phase term of β corresponds to a transfer function, $\exp(-j\beta)$. The filter responses at the two ports are given by

$$G_{\text{out}}(z) = -j[\exp(-j\beta)A_U(z) + \exp(j\beta)A_L(z)]/2 \quad (1)$$

$$H_{\text{out}}(z) = [\exp(-j\beta)A_U(z) - \exp(j\beta)A_L(z)]/2\cdot \quad (2)$$

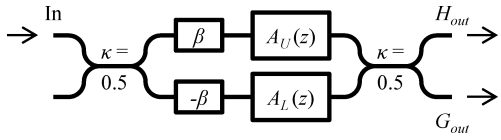

Fig. 1. High-level digital building block.

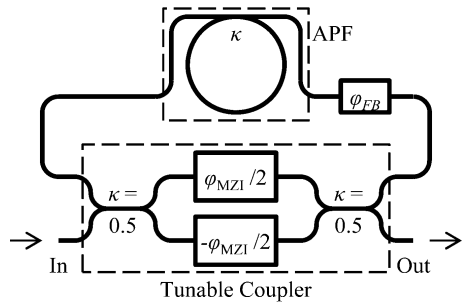

Fig. 2. Optical unit cell architecture.

B. Optical Unit Cell Architecture

Fig. 2 shows our optical unit cell architecture. This optical unit cell is used as the basic building block in all of our optical filter architectures. The tunable coupler provides tuning of the pole magnitude. The unit delay is uniquely provided by an "APF" microdisk resonator [4], which introduces frequency-dependent group delay and causes the optical response to deviate from a constant-group-delay digital filter response.

Manuscript received July 20, 2010; revised September 28, 2010; accepted October 21, 2010. Date of publication October 28, 2010; date of current version November 29, 2010. This work was supported in part by the Defense Advanced Research Projects Agency Si-PhASER Program under Grant 2106ATG Georgia-Tech through Michael W. Haney.

R. Patnaik and C. K. Madsen are with the Electrical and Computer Engineering Department, Texas A&M University, College Station, TX 77843 USA (e-mail: rpatnaik@tamu.edu; cmadsen@tamu.edu).

V. Vandrasi was with the Electrical and Computer Engineering Department, Texas A&M University, College Station, TX 77843 USA. He is now with CGGVeritas, Houston, TX 77072 USA (e-mail: vivek.vandrasi@cggveritas.com).

A. A. Eftekhar and A. Adibi are with the School of Electrical and Computer Engineering, Georgia Institute of Technology, Atlanta, GA 30332 USA (e-mail: eftekhar@ece.gatech.edu; adibi@ece.gatech.edu).

Digital Object Identifier 10.1109/JLT.2010.2089972

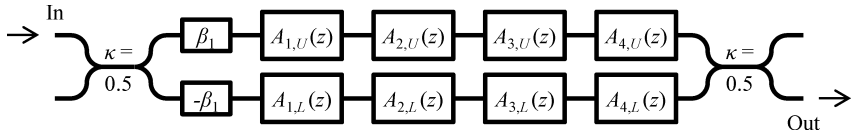

Fig. 3. High-level baseline filter architecture: 8 unit cells × 1 stage.

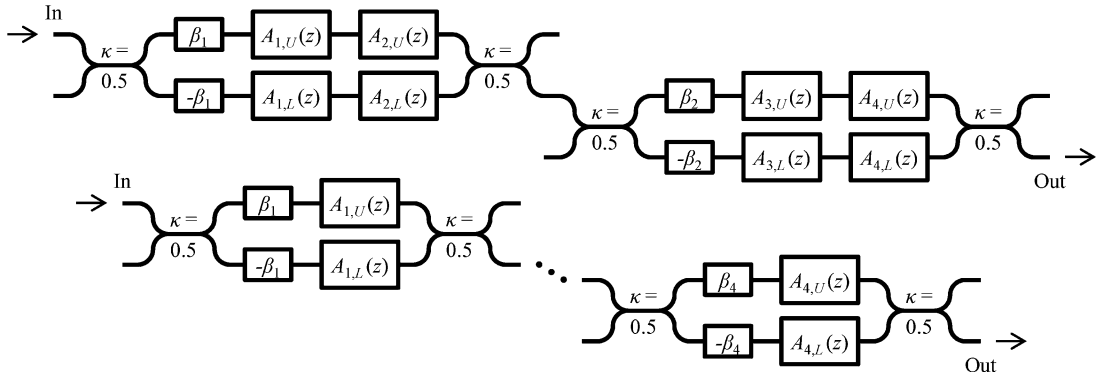

Fig. 4. High-level cascade filter architectures: 4 unit cells × 2 stages (top) and 2 unit cells × 4 stages (bottom).

In Fig. 2, if the tunable coupler is viewed as a simple MZI, then the two input ports (X_1 and X_2) and the two output ports (Y_1 and Y_2) are related by the equation

$$\begin{bmatrix} Y_1 \\ Y_2 \end{bmatrix} = \begin{bmatrix} H_{11} & H_{12} \\ H_{21} & H_{22} \end{bmatrix} \begin{bmatrix} X_1 \\ X_2 \end{bmatrix}. \tag{3}$$

The transfer function of the optical unit cell is then given by

$$\frac{Y}{X} = \frac{H_{22} - (H_{11}H_{22} - H_{12}H_{21})H_{\text{wvg}}\exp(-j\varphi_{fb})H_{\text{APF}}}{1 - H_{11}H_{\text{wvg}}\exp(-j\varphi_{fb})H_{\text{APF}}} \tag{4}$$

where H_{wvg} is the combined transfer function of the two waveguide connectors between the tunable coupler and the APF. For lossless optical components, $|H_{11}H_{22} - H_{12}H_{21}| = 1$. For an ideal constant group delay, $H_{\text{APF}} = z^{-1}$. In our analysis, the frequency-dependent linearly varying component of the phases for H_{wvg} and H_{11} are included in z^{-1}. (These increase the group delay in the feedback path by approximately a constant.) Given a high-level digital pole, pole_{dig} , for $A_U(z)$ or $A_L(z)$, the values for φ_{MZI} and φ_{fb} are given by

$$\varphi_{\text{MZI}} = 2\arcsin(|\text{pole}_{\text{dig}}|) \qquad \varphi_{fb} = -(\angle\text{pole}_{\text{dig}} + \pi/2). \tag{5}$$

i.e., they are related to the magnitude $|\text{pole}_{\text{dig}}|$ and the angle $\angle\text{pole}_{\text{dig}}$, respectively, of the digital pole.

We assume that all optical components are lossless; this allows for ease of mapping the digital parameters to the optical parameters. If lossy optical components are considered, then the magnitude response of the optical unit cell will exhibit frequency dependence (more specifically, a notch response); in this case, a constant magnitude response in the feedback path cannot be assumed as is the case for the digital design.

C. High-Level Digital Filter Architectures

All of our digital filter architectures are eight-zero-eight-pole designs. Fig. 3 shows the "baseline" architecture. In Fig. 3, each $A_{i,U}(z)$ or $A_{i,L}(z)$ is a single-zero-single-pole all-pass filter. Of all the high-level digital filter architectures presented in this paper, the baseline architecture has the fewest number of independent parameters.

Fig. 4 shows the cascade filter architecture; we consider two types of cascade filter architecture based upon the number of unit cells in each stage and the number of stages. We denote each architecture as the number of unit cells in each stage times the number of stages. Thus, in Fig. 4, the architectures are labeled as 4 unit cells × 2 stages and 2 unit cells × 4 stages, respectively, or 4×2 and 2×4 for simplicity. Since each stage has a separate β phase term, the 2×4 cascade architecture has more independent parameters than the 4×2 cascade architecture does. However, there are more unused output ports in the 2×4 cascade architecture than in the 4×2 cascade architecture (four versus two). The overall filter response is obtained by calculating the product of the filter responses of the individual stages. The cascade architecture has the advantage that each stage can be designed independently.

Fig. 5 shows the lattice filter architectures. There is a separate power coupling ratio κ_i for each stage. Note that this κ_i is different from the κ of the microdisk in Fig. 2. The 2×4 lattice architecture has more β phase terms as well as κ_i terms than the 4×2 lattice architecture does. Compared to the cascade architecture, the lattice architecture has fewer unused output ports. However, different stages of the lattice architecture cannot be designed independently as can be done in the cascade architecture, as we now discuss.

For the lattice architecture, both output ports of one stage are coupled to both input ports of the following stage. Since the filter response of each stage is determined by the relative contribution of both of its inputs, the optimal parameters for stage $i+1$ are dependent on those for stage i. This propagating effect means that

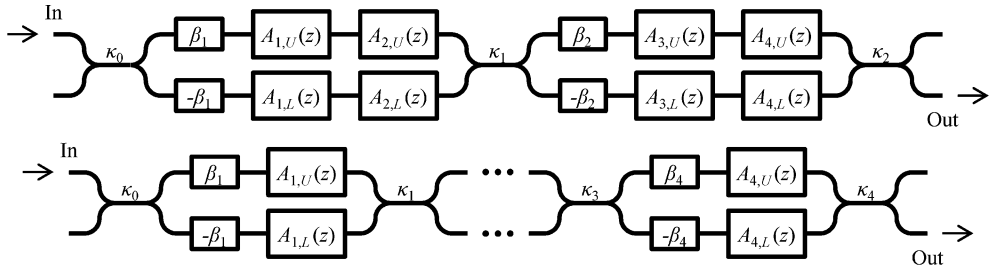

Fig. 5. High-level lattice filter architectures: 4 unit cells $\times$ 2 stages (top) and 2 unit cells $\times$ 4 stages (bottom).

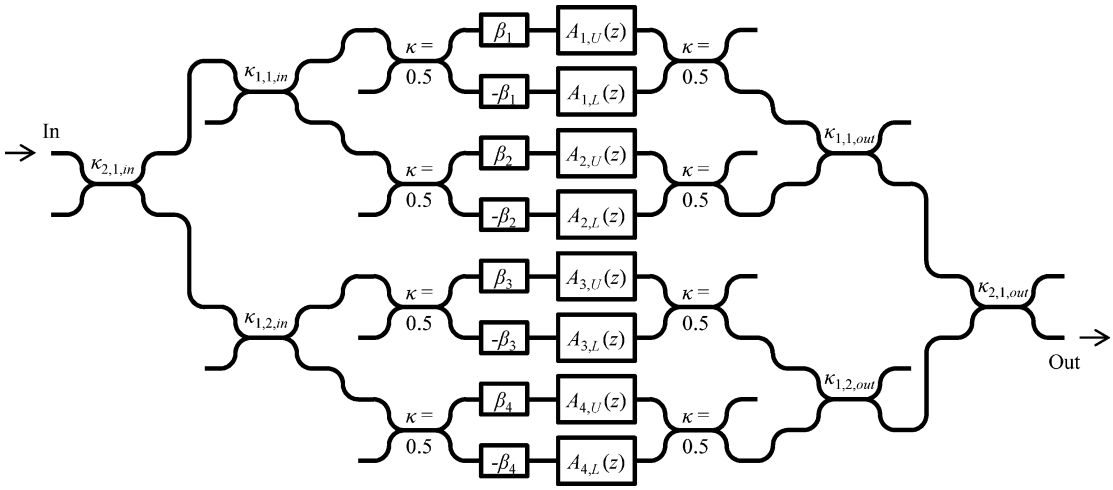

Fig. 6. High-level parallel filter architecture: 2 unit cells $\times$ 4 stages.

changing the parameters of one stage significantly affects the filter responses of all subsequent stages. Thus, the complexity of selecting the optimal parameters for a lattice architecture significantly increases as the number of stages is increased. In contrast, for the cascade architecture, the filter response, i.e., the input to output transfer function, of one stage, does not depend on the filter response of any previous stage. Thus, each of its stages can be designed independently.

Fig. 6 shows the 2×4 parallel filter architecture. The 4×2 architecture is similar to the top-half of the 2×4 architecture with $A_{1,U}(z)$ replaced by $A_{1,U}(z)A_{2,U}(z)$, $A_{2,U}(z)$ replaced by $A_{3,U}(z)A_{4,U}(z)$, etc. The number of κ_i terms is $2(\#\text{stages}) - 2$. The number of unused output ports is now $2(\#\text{stages}) - 1$. Thus, the parallel filter architecture has the largest number of unused output ports. The overall filter response is the weighted sum of the filter responses of the individual stages. Thus, the shaping of the overall filter response is achieved by filter averaging rather than by filter multiplication.

III. Simulation Results

We wish to use these filter architectures as channelizers, i.e., to extract a narrow range of optical frequencies from a large spectrum. (This will reduce the sampling rate needed for the subsequent analog-to-digital converter.) Thus, we designed each high-level digital filter architecture to produce a band-pass response (50 MHz bandwidth out of 10 GHz) with the desired magnitude responses in the passband and the stopband. In filter synthesis, we constrain the maximum pole magnitude to be at most 0.98 (i.e., smaller than one), and we optimize the values of the pole magnitudes and phases, the constant phase term β, and the power coupling ratios (for the lattice and parallel architectures) to best approximate the desired magnitude filter response. We refer to this procedure as "constrained pole optimization."

We now discuss our motivations to constrain the maximum pole magnitude to 0.98. First, as noted in Section II-B, we assume that all optical components are lossless. However, in real optical systems, there is always some loss present, and the loss in the feedback path sets an upper bound on the maximum pole magnitude. Second, for adequate control of the system, the poles should not be very close to the unit circle; otherwise, the system can become unstable due to parameter variations. Note that a passive system will remain stable, whereas if active gain is present, then the system may exhibit lasing. An important point to note is that a lossless system designed with a pole magnitude constrained to some value, e.g., 0.98, is not equivalent to a lossy system that is designed, assuming that the feedback pack has a magnitude response, $\gamma = 0.98$; this is because in a lossy system, the magnitudes of the poles as well as the zeros decrease by a factor γ.

In constrained pole optimization, we write the transfer function for each high-level digital filter architecture in terms of the aforementioned filter parameters. We then select weights for the relative errors in the passband and stopband, and we use the MATLAB function *fmincon* to perform multivariable constrained minimization.

TABLE I
OPTIMIZED PARAMETERS FOR THE HIGH-LEVEL BASELINE (8 × 1) AND CASCADE FILTER ARCHITECTURES

Type	$\lvert p_{1,U}\rvert, \angle p_{1,U}$	$\lvert p_{2,U}\rvert, \angle p_{2,U}$	$\lvert p_{3,U}\rvert, \angle p_{3,U}$	$\lvert p_{4,U}\rvert, \angle p_{4,U}$	$\beta_{1,U}$	$\beta_{2,U}$	$\beta_{3,U}$	$\beta_{4,U}$
8x1	0.9800, -0.0216	0.9730, 0.0345	0.9800, -0.0225	0.9698, -0.0032	1.5698			
4x2	0.9800, -0.0265	0.0967, 1.6150	0.9224, 0.0113	0.9800, -0.0272	-3.1416	1.5777		
2x4	0.9800, 0.0260	0.9800, 0.0260	0.9800, -0.0260	0.9800, -0.0260	-1.3915	1.7498	1.3916	1.3914

TABLE II
OPTIMIZED PARAMETERS FOR THE HIGH-LEVEL LATTICE FILTER ARCHITECTURES

Type	$\lvert p_{1,U}\rvert, \angle p_{1,U}$	$\lvert p_{2,U}\rvert, \angle p_{2,U}$	$\lvert p_{3,U}\rvert, \angle p_{3,U}$	$\lvert p_{4,U}\rvert, \angle p_{4,U}$	$\beta_{1,U}$	$\beta_{2,U}$	$\beta_{3,U}$	$\beta_{4,U}$
4x2	0.9737, 0.0348	0.9800, -0.0226	0.9761, 0.0023	0.9800, 0.0226	0.1392	0.1402		
2x4	0.9800, -0.0190	0.9800, 0.0205	0.9800, 0.0217	0.9800, 0.0216	-0.5862	-0.8438	-0.0147	1.0146
Type	κ_0	κ_1	κ_2	κ_3		κ_4		
4x2	0.5001	1.0000	0.4999					
2x4	0.9217	0.4950	0.6593	0.6349		0.5329		

TABLE III
OPTIMIZED PARAMETERS FOR THE HIGH-LEVEL PARALLEL FILTER ARCHITECTURES

Type	$\lvert p_{1,U}\rvert, \angle p_{1,U}$	$\lvert p_{2,U}\rvert, \angle p_{2,U}$	$\lvert p_{3,U}\rvert, \angle p_{3,U}$	$\lvert p_{4,U}\rvert, \angle p_{4,U}$	$\beta_{1,U}$	$\beta_{2,U}$	$\beta_{3,U}$	$\beta_{4,U}$
4x2	0.9800, 0.0228	0.9800, -0.0228	0.9800, 0.0228	0.9800, 0.0228	0.0004	-3.0303		
2x4	0.3449, 0.4177	0.4935, -0.6285	0.9800, 0.0210	0.7432, -0.6187	-2.4579	1.9302	-1.5689	1.5116
Type	$\kappa_{1,1,in}$	$\kappa_{1,2,in}$	$\kappa_{2,1,in}$	$\kappa_{1,1,out}$	$\kappa_{1,2,out}$		$\kappa_{2,1,out}$	
4x2	0.4996			0.4975				
2x4	0.4601	0.0005	0.9992	0.5399	0.9995		0.0008	

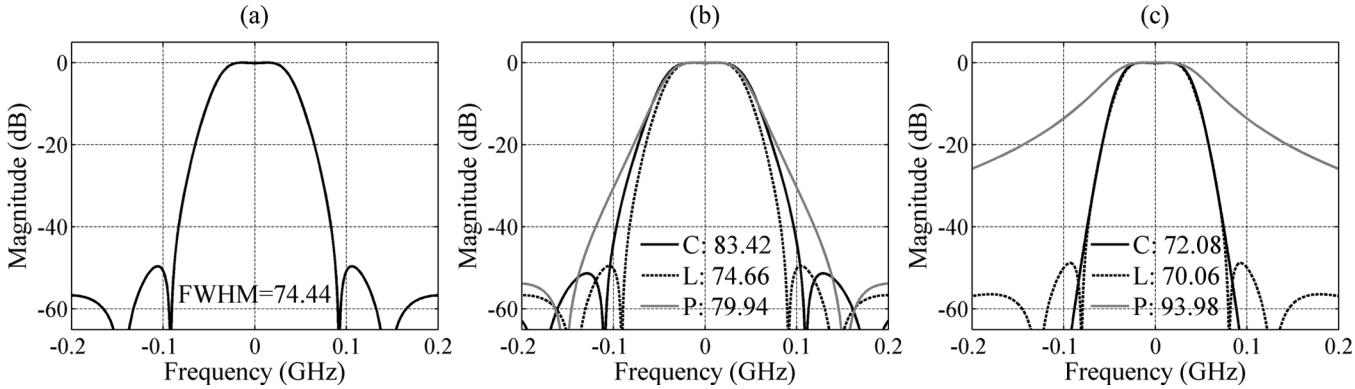

Fig. 7. Magnitude responses of the baseline, cascade (C), lattice (L), and parallel (P) optical filters. The FWHM values (in megahertz) are also noted. (a) Baseline (8 × 1). (b) 4 × 2 designs. (c) 2 × 4 designs.

Tables I–III show the values of the optimized parameters for the different architectures (all angles are in radians). The interested user can use these data to reconstruct the overall digital filter responses for the different architectures.

To obtain the optical filter response, the power coupling ratio κ for the microdisk was selected so that the sum of the group delays for the components in the feedback path (i.e., $H_{11}, H_{\rm wvg}$, and $H_{\rm APF}$) is the desired value of 100 ps (i.e., 1/10 GHz) at the central frequency. We assume that the mircrodisk has a radius of 20 μm [4]; for this microdisk size, the required value of κ is 0.07. To obtain the optical filter response, we also derived the values of the other optical parameters, as noted in Section II-B.

Fig. 7 shows the magnitude responses of the different optical filters. In Fig. 7, we note the full width at half maximum (FWHM), i.e., the distance between the points on the graph at which the magnitude response is 3-dB below its maximum value. From Fig. 7, we see that apart from the 2 × 4 parallel filter, all filters have similar FWHM values (between 70.06 and 83.42 MHz). The 2 × 4 lattice filter has the smallest FWHM value (70.06 MHz), whereas the 2 × 4 parallel filter has the largest FWHM value (93.98 MHz). As noted in Section II-C, the overall filter response for the parallel filter is the weighted sum of the filter responses of the individual stages. Thus, the FWHM is primarily determined by the number of unit cells in one stage. This is why the 2 × 4 parallel filter (only two unit cells per stage) has the largest FWHM. In contrast, the 4 × 2 parallel filter (four unit cells per stage) has a noticeably smaller FWHM. The lattice architecture appears to be promising in terms of producing lower FWHM values, but optimizing its design for a larger number of stages is difficult, as was discussed in Section II-C.

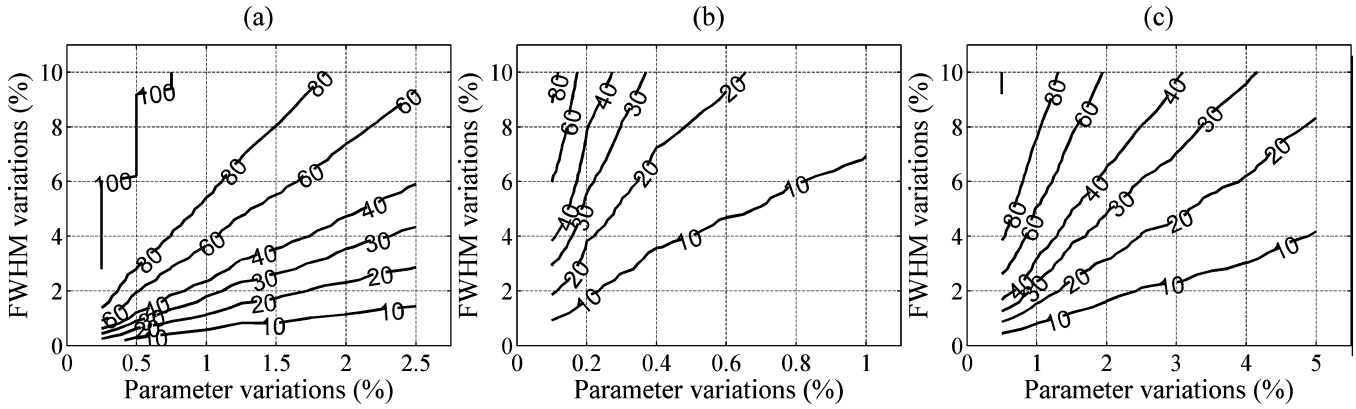

Fig. 8. Tolerance contour curves for the baseline (8×1) optical filter. The graphs show the expected percentage of samples for which the FWHM variations are within the percentages noted for the range of parameter variations noted. (a) ϕ_{MZI}. (b) ϕ_{fb}. (c) κ_{TC}.

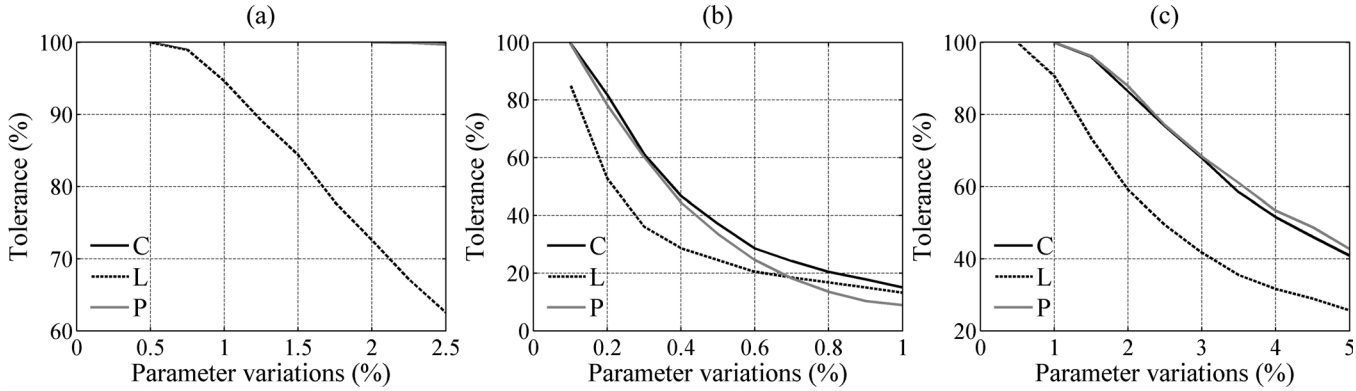

Fig. 9. Tolerance curves for the cascade (C), lattice (L), and parallel (P) 4×2 optical filters. The graphs show the expected percentage of samples for which the FWHM is within 10% of its nominal value for the range of parameter variations noted. (a) ϕ_{MZI}. (b) ϕ_{fb}. (c) κ_{TC}.

IV. Filter-Tolerance Tests

In this section, we examine the sensitivity of the different filter architectures to parameter variations via computer simulations. We first vary the tunable parameters of each optical unit cell, i.e., $\varphi_{\mathrm{MZI}}, \varphi_{fb}$, and the κ of the tunable coupler (which we denote as κ_{TC}); later, we vary the fixed parameter κ of each microdisk (which we denote as κ_{disk}). We vary these parameters by different random amounts (as a percentage of the nominal value), and we measure several characteristics of the overall filter response, specifically, the maximum passband gain and the FWHM value; the parameters of the different optical unit cells are varied by different amounts.

We note that another method to measure filter sensitivity is to vary the digital pole magnitudes and phases of each unit cell. The method we use in this paper should produce a more realistic estimate of the filter sensitivity. We note that both κ terms of tunable coupler are varied by the same amount. This is realistic because of their spatial proximity, which means that independent variations are less likely to occur than would be the case for couplers that were farther apart.

We calculate the percentage variation in the FWHM value and set a threshold for the maximum allowable variation. The value of this threshold is then used to calculate the tolerance curves for the different optical filters. Since significant variations in the maximum passband gain did not occur, we did not use this metric to obtain the tolerance curve. Fig. 8 shows the tolerance contour curves for the baseline optical filter; the graphs in Fig. 8 show the expected percentage of samples for which the FWHM variations are within the percentages noted for the range of parameter variations noted. We now make several comments about the data in Fig. 8. Since the tolerance contours are approximately straight lines, the FWHM value variations are approximately a linear function of the parameter variations. The optical filter is most sensitive to variations in φ_{fb} , then to variations in κ_{TC}, and then to variations in φ_{MZI}. From (5), we see that changing φ_{MZI} changes the pole magnitude, whereas changing φ_{fb} changes the pole phase. Thus, the optical filter is most sensitive to variations in the pole phase and is least sensitive to variations in the pole magnitude. We note that changing κ_{TC} changes the zero locations of H_{out} in (2) and only changes the magnitude of G_{out} in (1).

We present filter-tolerance test results for the other optical filters considering 10% as the maximum acceptable variation in the FWHM from its nominal value. Fig. 9 shows the tolerance curves for the 4×2 architectures. Fig. 10 shows the tolerance curves for the 2×4 architectures. The graphs in Figs. 9 and 10 show the expected percentage of samples for which the FWHM is within 10% of its nominal value for the range of parameter variations noted. In Fig. 9(a), the graphs for the cascade and parallel optical filters are approximately at 100%, and in Fig. 10(a), the graph for the parallel optical filter is approximately at 100%.

We first discuss the data in Fig. 9. We see that the curves for the cascade and parallel optical filters are very similar, whereas the curve for the lattice optical filter lies noticeably below the

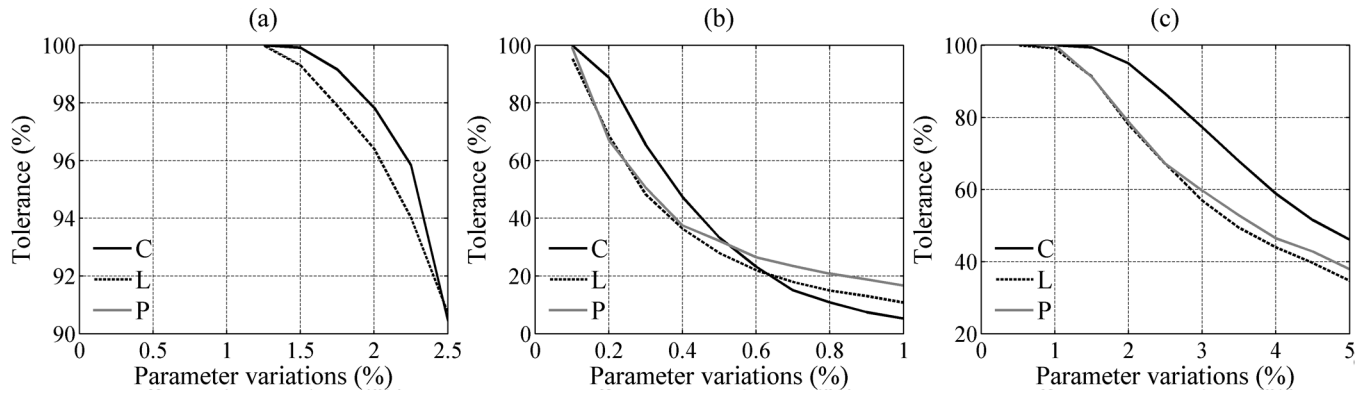

Fig. 10. Tolerance curves for the cascade (C), lattice (L), and parallel (P) 2×4 optical filters. The graphs show the expected percentage of samples for which the FWHM is within 10% of its nominal value for the range of parameter variations noted. (a) ϕ_{MZI}. (b) ϕ_{fb}. (c) κ_{TC}.

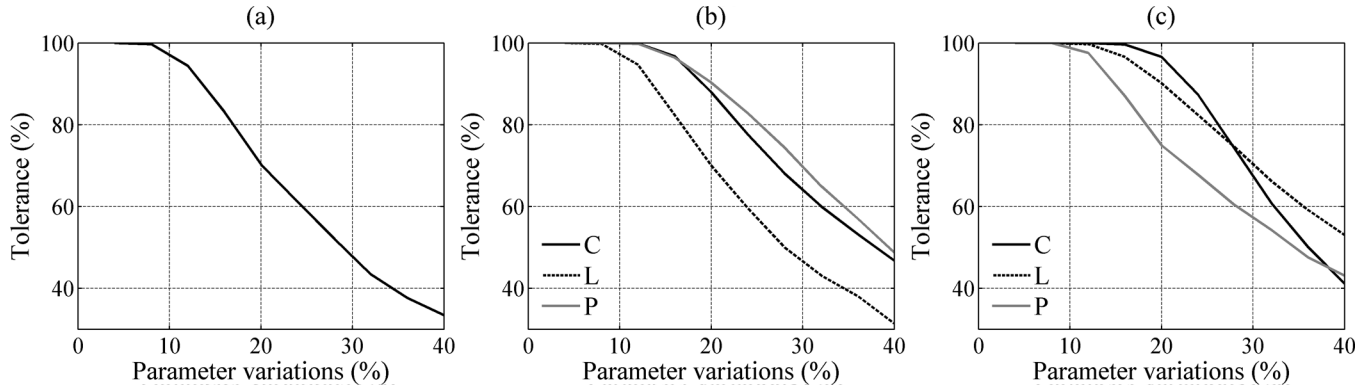

Fig. 11. Tolerance curves for variations in κ_{disk} disk for the baseline, cascade (C), lattice (L), and parallel (P) optical filters. The graphs show the expected percentage of samples for which the FWHM is within 10% of its nominal value for the range of parameter variations noted. (a) Baseline. (b) 4×2 (c) 2×4.

other curves. Thus, the lattice optical filter has the worst tolerance to parameter variations. We next discuss the data in Fig. 10. For variations in φ_{MZI}, the parallel optical filter now has the best tolerance, whereas for variations in φ_{fb} and κ_{TC}, the cascade optical filter generally has the best tolerance. From the aforementioned analysis, we conclude that the cascade optical filter generally has the best tolerance to parameter variations, whereas the lattice optical filter generally has the worst tolerance to parameter variations. We note that the tolerance tests in this paper are an indication of the tolerances of the actual optical devices. Here, we are not concerned with numerical stability issues that one may encounter in the design of digital filters where quantization and round-off errors are of concern, especially for fixed-point arithmetic. In such cases [5], [6], the metrics used to measure tolerance are different, and thus, so are the conclusions.

For completeness, we now present tolerance curves for variations in κ_{disk} in Fig. 11. Recall (see Section III) that $\kappa_{\mathrm{disk}} = 0.07$; this is much smaller than the 0.5 value used for κ_{TC}. We note that decreasing (increasing) κ_{disk} increases (decreases) the height and sharpness of the group delay response of the feedback path; the resulting response for one unit cell becomes narrower (wider). We now discuss the data in Fig. 11. For up to a 10% range of parameter variations, all curves are at 100% or close to 100%. We select a 20% range of parameter variations as the operating point at which to compare the different filter architectures. At this operating point, the tolerance values are: baseline (70.30%), 4×2 cascade (87.94%), 4×2 lattice (69.98%), 4×2 parallel (90.28%), 2×4 cascade (96.6%), 2×4 lattice (90.14%), and 2×4 parallel (74.94%). The cascade optical filters again seem to have the best tolerance. There is no clear trend for the lattice and parallel optical filters for variations in κ_{disk}.

To compare the different optical filters, we also calculated the circulating power in the microdisks using the method in [7]; the greater the circulating power, the greater are the distortions due to nonlinearity effects. Table IV shows the circulating power (in milliwatt), assuming that power input to the optical filter is 1 mW. Since the circulating power in a microdisk is a function of both the pole magnitude and the power input to the corresponding unit cell, different microdisks with the same pole magnitude can have very different circulating powers, e.g., for both the cascade and lattice 2×4 optical filters, $|p_{3,U}| = 0.98$, but the values for the circulating power are 2710 and 4250 mW, respectively.

From Table IV, we see that the 4×2 parallel optical filter has the smallest value of the largest circulating power in any microdisk (1370 mW). Thus, the 4×2 parallel filter architecture is the best among the ones considered to minimize nonlinearity effects. From Figs. 9 and 11(b), we see that the tolerance curves for the 4×2 cascade and 4×2 parallel optical filters are very similar. Thus, if simultaneous tolerance to parameter sensitivity and minimization of nonlinearity effects are desired, then the 4×2 parallel filter architecture is the most suitable one. We note that six out of eight microdisks for the 2×4 parallel optical filter have circulating power values of at most 0.1 mW. However,

TABLE IV
CIRCULATING POWER (IN MILLIWATT) IN THE DIFFERENT MICRODISKS OF THE VARIOUS OPTICAL FILTERS

Type	$1,U$	$1,L$	$2,U$	$2,L$	$3,U$	$3,L$	$4,U$	$4,L$
Baseline	2730	2730	2020	2020	2730	2730	1800	1800
4x2 Cascade	2730	2730	33.5	33.5	683	683	2730	2730
4x2 Lattice	2070	2070	2730	2730	2280	2280	2730	2730
4x2 Parallel	1370	1370	1370	1370	1360	1360	1360	1360
2x4 Cascade	2730	2730	2720	2720	2710	2710	2690	2690
2x4 Lattice	4280	5040	3120	2350	4250	1220	2850	2610
2x4 Parallel	0.0247	0.0247	0.0302	0.0302	2730	2730	0.101	0.101

The power input to the optical filter is assumed to be 1 mW. The greater the circulating power, the greater are the distortions due to nonlinearity effects.

two of the microdisks have a circulating power value of 2730 mW. This large range of values is a result of most of the input power being directed to the third stage (based on the selection of the optimized κ values for the lattice architecture). In general, to minimize the effects of nonlinearity of an already designed system, we would place the unit cells with the largest (smallest) pole magnitudes where the input power is the smallest (largest).

We note that [7] has a method to calculate the effective nonlinear phase shift versus the phase shift of a ring resonator. For the data presented in Table IV, there is a linear relation between the circulating power in a silicon microdisk and the effective nonlinear phase shift. Thus, the greater the circulating power, the greater is the shift in the microdisk phase and thus in the microdisk center frequency.

We now make several concluding remarks. We note that with the use of a smaller maximum pole magnitude in constrained pole optimization, we expect the filter sensitivity to parameter variations to decrease for all filter architectures considered; however, for the purposes of comparing the sensitivities of different filter architectures, the 0.98 value of the maximum pole magnitude should be adequate. Our choice of this 0.98 value was discussed in Section III. We also note that we compared cascade, lattice, and parallel filter architectures using a regular structure, e.g., 4×2 or 2×4, i.e., with the same number of unit cells in each stage. Our conclusions should be valid for filter architectures with a larger number of total unit cells if this regular structure is maintained. However, if different numbers of unit cells are used in different stages, then our conclusions may not be applicable.

REFERENCES

[1] C. K. Madsen, "Efficient architectures for exactly realizing optical filters with optimum band-pass designs ," *IEEE Photon. Technol. Lett.*, vol. 10, no. 8, pp. 1136–1138, Aug. 1998.

[2] K. Jinguji, "Synthesis of coherent two-port optical delay-line circuit with ring waveguides," *J. Lightw. Technol.*, vol. 14, no. 8, pp. 1882 –1898, Aug. 1996.

[3] C. K. Madsen and J. H. Zhao, *Optical Filter Design and Analysis: A Signal Processing Approach*. New York : Wiley, 1999, chs. 4–6.

[4] Q. Li, S. Yegnanarayanan, A. Eftekhar, and A. Adibi, "Low-loss microdisk-based delay lines for narrowband optical filters," presented at the Integrated Photonics Research Silicon and Nanophotonics, OSA Technical Digest (CD) (Optical Society of America, 2010), Paper IMC7.

[5] K. Erickson and A. Michel, "Stability analysis of fixed-point digital filters using computer generated Lyapunov functions—Part I: Direct form and coupled form filters," *IEEE Trans. Circuits Syst.*, vol. CAS-32, no. 2, pp. 113–132, Feb. 1985.

[6] K. Erickson and A. Michel, "Stability analysis of fixed-point digital filters using computer generated Lyapunov functions—Part II: Wave digital filters and lattice digital filters," *IEEE Trans. Circuits Syst.*, vol. CAS-32, no. 2, pp. 132–142, Feb. 1985.

[7] J. E. Heebner and R. W. Boyd, "Enhanced all-optical switching by use of a nonlinear fiber ring resonator," *Opt. Lett.*, vol. 24, no. 12, pp. 847–849, Jun. 1999.

Author biographies not included at authors' request due to space constraints.